Title

A Hierarchy of Idealized Monsoons in an Intermediate GCM A Hierarchy of Idealized Monsoons in an Intermediate GCM

Journal

Journal of Climate, 31(22)

ISSN

0894-8755

Authors

Zhou, Wenyu
Xie, Shang-Ping

Publication Date

2018

DOI

10.1175/jcli-d-18-0084.1

Peer reviewed

A Hierarchy of Idealized Monsoons in an Intermediate GCM

Wenyu Zhou *and* Shang-Ping Xie

Scripps Institution of Oceanography, University of California, San Diego, La Jolla, California

Abstract

A hierarchy of idealized monsoons with increased degrees of complexity is built using an intermediate model with simplified physics and idealized land–sea geometry. This monsoon hierarchy helps formulate a basic understanding about the distribution of the surface equivalent potential temperature θ_e, which proves to provide a general guide on the monsoon rainfall. The zonally uniform monsoon in the simplest aquaplanet simulations is explained by a linearized model of the meridional distribution of θ_e, which is driven by the seasonally varying solar insolation and damped by both the monsoon overturning circulation and the local negative feedback. The heat capacities of the surface and the atmosphere give rise to an intrinsic time scale that causes the monsoon migration to lag behind the sun and reduces the monsoon extent and intensity. Monsoons with a zonally confined continent can be understood based on the zonally uniform monsoon by considering the ocean influence on the land through the westerly jet advection, which reduces the monsoon extent and induces zonal asymmetry. Monsoon responses to more realistic factors such as land geometry, albedo, and ocean heat flux are consistently predicted by their impacts on the surface θ_e distribution. The soil moisture effect, however, does not fully fit into the surface θ_e argument and provides additional control on monsoon rainfall by inducing regional circulation and rainfall patterns.

Keywords: Atmosphere-land interaction; Monsoons; Climate models

1. Introduction

Monsoons are important components of the global climate system and deliver much-needed rain to billions of people. Understanding monsoon dynamics is of broad scientific and socioeconomic importance.

The observed monsoon manifests a meridional circulation that accounts for most of the cross-equatorial flow in the zonal-mean Hadley circulation during the solstice seasons (Dima and Wallace 2003). The dry, axisymmetric Hadley circulation theory (Held and Hou 1980; Lindzen and Hou 1988; Plumb and Hou 1992) has been applied to understand monsoon dynamics (Chao and Chen 2001; Gadgil 2003; Privé and Plumb 2007a), viewing the monsoon as a thermally direct circulation driven by the diabatic heating from precipitation over subtropical land. The peak ascent is found to be located just equatorward of the free-tropospheric temperature maximum.

The dry theory, however, does not explain what determines the distributions of precipitation and the associated diabatic heating. One can instead consider monsoons in a moist framework where precipitation becomes an

internal variable. In particular, precipitation is related to the surface equivalent potential temperature θ_e under the quasi-equilibrium assumption of moist convection, which relaxes the atmosphere toward a state of convective neutrality. Combining the quasi-equilibrium assumption with the dynamical constraints on the Hadley circulation, the free-tropospheric temperature maximum becomes collocated with the surface θ_e maximum, and the peak ascent sits just equatorward of the surface θ_e maximum (Emanuel 1995; Privé and Plumb 2007a; Neelin 2007; Nie et al. 2010). As shown in Fig. 1, the surface θ_e distribution works well to explain the rainfall extents of observed monsoons. However, the theory remains diagnostic as an understanding on what sets the basic distribution of θ_e is still lacking.

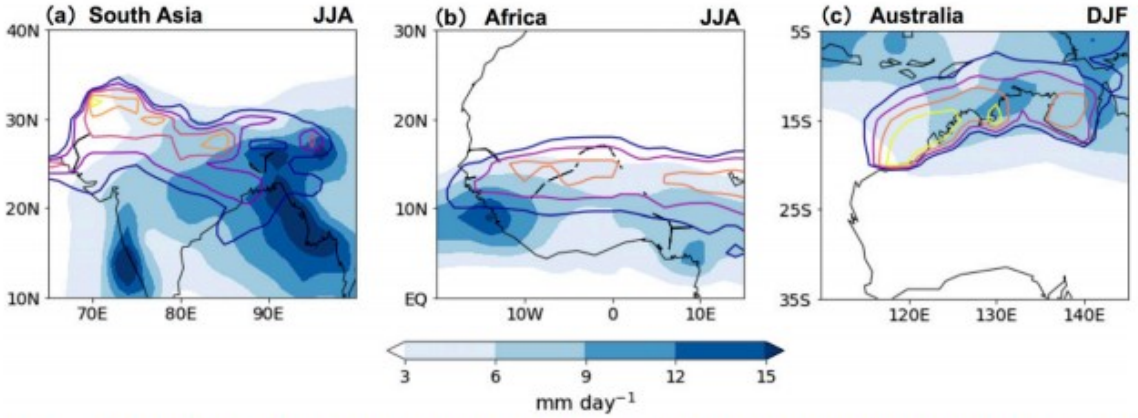

FIG. 1. Spatial distribution of the seasonal-mean precipitation (shading; GPCP) and surface θ_e (contours; evaluated at 2 m from the surface using ERA-Interim) for (a) South Asia (θ_e contours start from 358 K with a 2-K interval), (b) Africa (θ_e contours start from 346 K with a 2-K interval), and (c) Australia (θ_e contours start from 352 K with a 1-K interval).

Another perspective to understand the cross-equatorial circulations is from the energetic constraint (e.g., Broccoli et al. 2006; Kang et al. 2008, 2009; Yoshimori and Broccoli 2009; Frierson and Hwang 2012; Frierson et al. 2013; Schneider et al. 2014; Boos and Korty 2016). In response to an energy source that produces a tendency of vertically integrated moist static energy, the circulation would change accordingly to transport the anomalous energy out. For example, the zonal-mean Hadley circulation tends to shift toward the hemisphere that receives more energy, and the monsoon extent has been shown to be limited by the zonal and meridional ventilation of the lower moist static energy air from cooler oceans (Chou and Neelin 2001; Chou et al. 2001; Privé and Plumb 2007b) and from the subtropics (Boos and Kuang 2010; Thorncroft et al. 2011; Zhai and Boos 2017), respectively. The energetic perspective should be internally consistent with the surface θ_e perspective. Abovementioned processes would also affect the θ_e distribution, but the detailed dynamical pathways remain to be revealed.

While simple theories are useful for understanding basic monsoon dynamics, the simplification may miss certain key processes that are essential for realistic monsoons. For example, the zonally confined continent induces an

extra west–east dimension (Rodwell and Hoskins 1996; Xie and Saiki 1999; Chou et al. 2001; Privé and Plumb 2007b) that is not considered by the zonally uniform monsoon theories. It is also not clear how the impacts of land surface properties (Meehl 1994; Dirmeyer 1998; Levine and Boos 2017; Zhou and Xie 2017; Berg et al. 2017) could be incorporated into the above monsoon theories. Conversely, because of the intrinsic complexity in physics and feedbacks, it is often difficult to isolate fundamental monsoon dynamics from direct diagnosis of global climate models (GCMs) and observations. Hence, there is a gap between simple theories and comprehensive GCMs/observations (Held 2005). This study aims to bridge this gap with an intermediate GCM that includes a reasonably realistic presentation of the monsoon but is still simple enough, in physics and geometry, for dynamical insights (e.g., Dirmeyer 1998; Xie and Saiki 1999; Chou and Neelin 2001; Chou et al. 2001; Privé and Plumb 2007a,b; Bordoni and Schneider 2008; Fučkar et al. 2013; Maroon et al. 2016; Maroon and Frierson 2016).

In particular, a hierarchy of idealized monsoons is built by adding complexity step by step, from the simplest aquaplanet monsoon over a uniform slab ocean to the more realistic monsoon over a subtropical continent that is zonally confined and has an interactive soil moisture scheme. The aquaplanet monsoon can be analytically explained by a linearized model of the interhemispheric temperature variation. Based on the aquaplanet monsoon, we further consider how the surface θ_e distribution is affected by more realistic components, such as meridionally nonuniform heat capacity, zonally confined continent extent, interactive soil moisture, land geometry, and local and remote forcings. Eventually, we formulate a basic understanding of the surface θ_e distribution, which in general guides monsoon rainfall features such as the extent, intensity, and time evolution.

The rest of the paper is organized as follows. Section 2 describes the datasets and the intermediate GCM used in this study. In section 3, aquaplanet monsoons are described, and an analytical solution is derived from a linearized model to explain their behaviors. In section 4, monsoons with a simple subtropical continent are simulated with increasing degrees of complexity. Their behaviors are understood based on simpler monsoons. Section 5 studies monsoon responses to local and remote forcings from the surface θ_e perspective. Section 6 is a summary.

2. Methods

a. Dataset

The monthly precipitation data from the Global Precipitation Climatology Project (GPCP; Adler et al. 2003) are used to estimate the realistic monsoon rainfall. The four-times-daily near-surface air temperature, humidity, and pressure are obtained from the ERA-Interim dataset (Dee et al. 2011) to compute the surface θ_e. The climatological mean from 1979 to 2005 is used.

b. Model and simulations

We use the gray-radiation moist GCM (Frierson 2007; O'Gorman and Schneider 2008). The model integrates the hydrostatic primitive equations using the spectral dynamical core of Geophysical Fluid Dynamics Laboratory (GFDL). The model includes a simple representation of the hydrological cycle with a simplified Betts–Miller convection scheme (Frierson 2007). The scheme relaxes the convectively unstable atmospheric columns toward a pseudoadiabatic temperature profile. The model employs a two-stream gray-radiation scheme, and the radiative effects of water vapor are not considered. A seasonally varying solar insolation without the diurnal cycle is used with a solar constant of 1360 W m^{-2} and an obliquity of 23.5°. Since there is no condensed water (i.e., clouds) in the atmosphere, the surface albedo is set uniformly at 0.38 (unless otherwise stated) to make surface temperatures close to observations. All simulations use the T43 spectral resolution in the horizontal and 13 unevenly spaced vertical levels.

For the aquaplanet simulations, we use a slab ocean with a uniform depth as the surface boundary condition (Bordoni and Schneider 2008). To represent the oceanic equatorial upwelling, a negative heat flux has been prescribed as follows (Merlis et al. 2013):

$$\mathrm{HFX} = -Q_0 \frac{1}{\cos\phi}\left(1-\frac{2\phi^2}{\phi_0^2}\right)\exp\left(-\frac{\phi^2}{\phi_0^2}\right), \qquad (1)$$

where ϕ is the latitude. The width and amplitude parameters are Q_0 = 50 W m^{-2} and ϕ_0 = 16°. This flattens the tropical sea surface temperature (SST) and eliminates the unrealistic strong SST and rainfall peak at the equator. The uniform depth of the slab ocean is varied widely to help conceptualize the aquaplanet monsoon. For the land simulation, a subtropical continent is placed in the Northern Hemisphere. The heat capacity of the land is set as equivalent to that of 0.1-m-deep water. The sensitivity to land soil moisture, land geometry, land albedo, and ocean heat flux is investigated by perturbing corresponding parameters. More details are given in the following sections. Table 1 lists abbreviated names and brief descriptions of all simulations.

TABLE 1. A summary of simulations.

Name	Aquaplanet simulation description
Aqua(H)	Slab-ocean depth of H m
Aqua0p1 + 7200days	Slab-ocean depth of 0.1 m and an artificially long year of 7200 days
Zonal-Moist	Zonally uniform land from 15° to 90°N; land is saturated with unlimited moisture for evaporation
Moist	Zonally confined saturated land that spans from 130° to 230°
Dry	Zonally confined dry land that reduces the evaporation to 10% of the potential evaporation
Land	Zonally confined land with interactive moisture (following experiments are all based on this experiment)
Wide	Wider land from 100° to 260°
Narrow	Narrower land from 150° to 210°
LN30	Land from 15° to 30°N
LS20	Land from 20° to 90°N
Alb1p2	20% increase in the land albedo
Alb0p8	20% decrease in the land albedo
NH-Flx	NH warming ocean heat flux
SH-Flx	SH cooling ocean heat flux

3. Aquaplanet simulations

Figure 2 shows the seasonal migration of the zonal-mean precipitation, surface θ_e, and surface winds in the aquaplanet simulations with widely varying slab-ocean depth H. In the Aqua50 simulation, the slab-ocean depth (50 m) is close to that of the realistic ocean mixed layer, the seasonal precipitation peak extends to ~10°N (Fig. 2b), resembling the observed zonal-mean precipitation. In the Aqua0p1 simulation, the slab-ocean depth (0.1 m) is close to the equivalent depth of the realistic land heat capacity; the seasonal precipitation is stronger and extends farther poleward (Fig. 2e), resembling the observed monsoon rainfall.

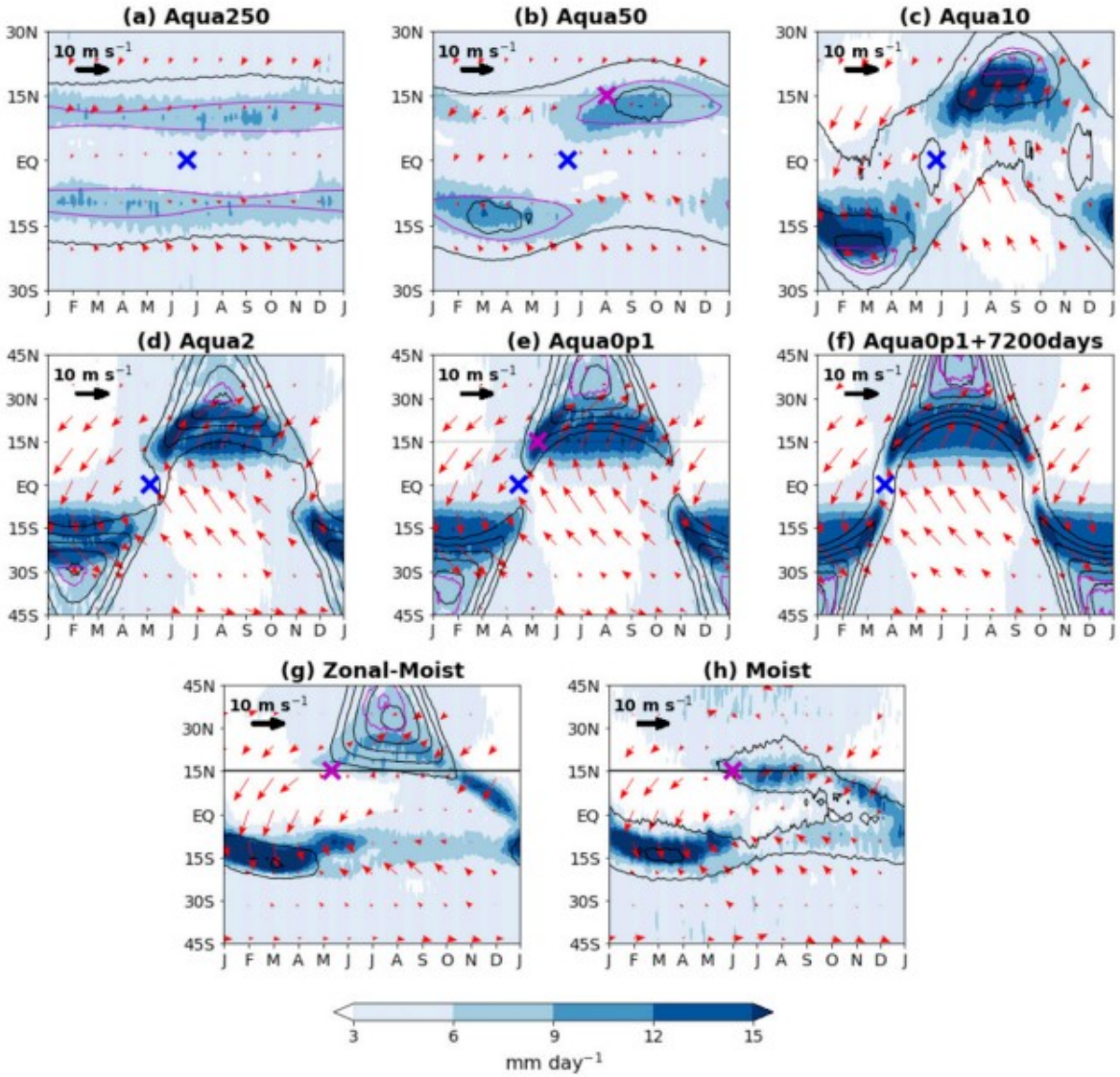

FIG. 2. Seasonal migrations of the zonal-/sector-mean precipitation (shading), surface θ_e (black contours; evaluated at the lowest model level; 6-K interval starting from 332.15 K) and surface air temperature (magenta contours; 1-K interval) in aquaplanet simulations with various slab-ocean depths H from (a) 250 to (e) 0.1 m. (f) The aquaplanet simulation achieved with an artificially long year of 7200 days that represents a simultaneous equilibrium with solar insolation. (g) The simulation achieved by adding a zonally uniform moist land into the aquaplanet of a 50-m slab ocean north of 15°N. (h) The sector-mean precipitation and θ_e averaged over the land longitudes in the simulation with a zonally confined moist land. The blue cross indicates the time of the precipitation shift when the NH tropical mean (0°–30°N) becomes larger than the SH tropical mean (0°–30°S). The magenta cross indicates the time when the precipitation averaged from 15° to 25°N (over the land if there is a zonally confined land) exceeds its annual mean.

In all simulations, monsoon rainfalls are well guided by the surface θ_e (back contours): The rainfall peak is located slightly equatorward of the θ_e maximum, and the rainfall intensity increases with the interhemispheric variation of θ_e. As H decreases from 250 to 0.1 m, monsoon rainfall extends farther poleward, shifts earlier (blue crosses) from the Southern Hemisphere (SH) to the Northern Hemisphere (NH), and intensifies. All these changes are consistently predicted by changes in the temporal–spatial distribution of the surface θ_e. With a saturated surface, the

surface θ_e is mainly controlled by the surface air temperature (magenta contours), despite a slight equatorward displacement due to the background moisture gradient. The extent, intensity, and time evolution of the monsoon rainfall can then be understood from the distribution of the surface air temperature.

We will first focus on the time evolution and intensity of the monsoon rainfall. Figure 3a confirms that the time evolution and intensity of the monsoon rainfall, as measured by the interhemispheric difference in the rainfall ΔP (light line), is well guided by the interhemispheric difference in the surface air temperature ΔT (bold line) in all aquaplanet simulations with various *H.* As *H* decreases from nearly infinite to negligible, ΔT_a shifts earlier, from late June to mid-April, and intensifies from nearly 0 to about 13 K. To understand such behavior, we build a linearized model of ΔT_a based on the energetic equations of the atmosphere and the slab ocean.

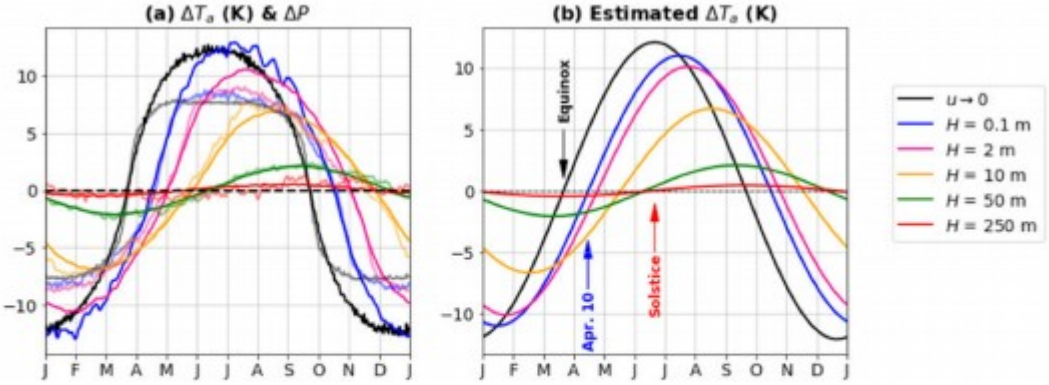

FIG. 3. (a) Time evolution of the difference between the NH tropical mean and the SH tropical mean in surface air temperature ΔT_a (thick line) and precipitation ΔP (thin line) for simulations with various slab-ocean depths H (color lines) and that in instant equilibrium with solar insolation with a negligible time scale u (black line). (b) Time evolution of the corresponding ΔT_a from the analytical solution of Eq. (11).

For the coupled atmosphere–slab-ocean column averaged over either the NH or the SH tropics (schematically shown in Fig. 4), the energetic equations can be linearized in terms of the surface air temperature anomaly T_a and the SST anomaly T_s from their annual-mean values, which are

$$C_{pa}\frac{dT_a}{dt} = \underbrace{-\beta T_a}_{\text{TOA radiation}} \underbrace{+\varepsilon(T_s - T_a)}_{\text{Surface flux}} \underbrace{-\alpha(T_a - \overline{T_a})}_{\text{Meridional mixing}}, \qquad (2)$$

and

$$C_{ps}\frac{dT_s}{dt} = \underbrace{S}_{\text{Absorbed solar}} \underbrace{-\varepsilon(T_s - T_a)}_{\text{Surface flux}}. \qquad (3)$$

The atmosphere is assumed to be in quasi equilibrium with T_a, so the change of its vertically integrated moist static energy with T_a can be estimated by a single heat capacity parameter C_{pa}. By assuming an opaque lower

troposphere for the longwave radiative flux and minimal change in the shortwave radiative flux with temperature, the change of the outgoing radiative flux at the top of the atmosphere with T_a is estimated by a feedback parameter β and the surface energy flux (sensible heat plus latent heat plus longwave) is parameterized by an exchange coefficient ε. The variable α represents the meridional mixing because of the monsoon overturning circulation that nudges T_a to the tropical-mean (30°S–30°N) value $\overline{T_a}$. The absorbed shortwave flux at the surface $S = (1 - \text{alb})S^{\downarrow}$ is the, where "alb" is the surface albedo and $S^{\downarrow}$ is the downward surface shortwave flux. The value of C_{pa} is estimated to be 2.2 × 10^7 J m^{-2} K^{-1}, which is close to that of 5-m-deep water. Please note that C_{pa} is larger than its dry part because of the increasing atmospheric moisture with temperature (Cronin and Emanuel 2013). The values ε and β are estimated to be 40 and 2 W m^{-2} K^{-1}, respectively (Nilsson and Emanuel 1999). The variable α is related to the overturning time scale of the meridional monsoon circulation τ_{ot} as $\alpha = C_{pa}/\tau_{\text{ot}}$ and is estimated to be 8 W m^{-2} K^{-1} by assuming $\tau_{\text{ot}} \cong 1\text{month}$ (Gonzalez and Rojas 2014). The variable C_{ps} is the surface heat capacity (J m^{-2} K^{-1}), which is a function of the slab-ocean depth *H*:

$$C_{ps} = 4.2 \times 10^6 H. \qquad (4)$$

Subtracting between the NH and the SH leads to

$$C_{pa}\frac{d\Delta T_a}{dt} = -\gamma \Delta T_a + \varepsilon(\Delta T_s - \Delta T_a) \qquad (5)$$

and

$$C_{ps}\frac{d\Delta T_s}{dt} = \Delta S - \varepsilon(\Delta T_s - \Delta T_a), \qquad (6)$$

where Δ means the tropical interhemispheric difference and $\gamma = \alpha + \beta = 10$ W m^{-2} K^{-1} represents the total meridional smoothing from both the monsoon overturning circulation and the local negative feedback. This formula is similar to that of the radiative–convective equilibrium problem studied in Cronin and Emanuel (2013), except that our system is forced by a time-varying forcing and that there are two boxes interacting with each other. In this coupled system, ΔT_a responds to ΔT_s on a time scale of $\tau_a = C_{pa}/(\varepsilon + \gamma)$, ΔT_s responds to ΔT_a on a time scale of $\tau_s = C_{ps}/\varepsilon$, and the integrated ΔT_a and ΔT_s respond to the forcing on a time scale of $\tau_c = (C_{pa} + C_{ps})/\gamma$. Given ε is much larger than γ, both τ_a and τ_s are much smaller than τ_c. This means that ΔT_s and ΔT_a can be seen as in quasi equilibrium with each other and respond together to the seasonal forcing on the time scale of τ_c. With this conceptual understanding in mind, we derive a more rigorous solution as follows. We first eliminate ΔT_s from Eqs. (5) and (6) and have

$$\frac{d\Delta T_a}{dt} + \frac{C_{ps}}{C_p}\frac{C_{pa}}{\varepsilon}\frac{d^2\Delta T_a}{dt^2} = \frac{\Delta S}{C_p} - \frac{\Delta T_a}{\tau}, \qquad (7)$$

where

$$C_p = C_{pa} + C_{ps}\frac{\varepsilon + \gamma}{\varepsilon} \qquad (8)$$

is the effective heat capacity of the coupled system, and

$$\tau = \frac{C_p}{\gamma} \qquad (9)$$

is the time scale for ΔT_a to achieve an equilibrium with the forcing. The second-order derivative term is much smaller than other terms because $C_{ps}/C_p < 1$, and the seasonal time scale of the varying solar insolation is much longer than that of $C_{pa}/\varepsilon \cong 6\,\text{days}$. One can then drop it and rewrite Eq. (7) as

$$\frac{d\Delta T_a}{dt} = \frac{\Delta S}{C_p} - \frac{\Delta T_a}{\tau}. \qquad (10)$$

The tropical interhemispheric difference of the surface absorbed solar radiation ΔS is a sine function of time as

$$\Delta S = S_o \sin\hat{t}, \qquad (11)$$

where S_o = 130 W m^{-2} is a scaling and $\hat{t} = (t/T)2\pi$ is the normalized time with t as the seconds from the March equinox and T as the total seconds in a year.

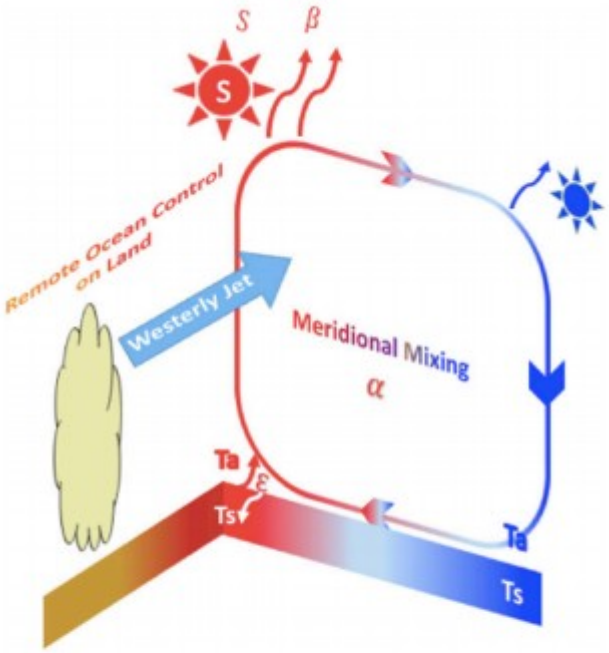

FIG. 4. A conceptual model for the surface temperature distribution. For the zonal-mean picture, the meridional variation in surface temperature is driven by the meridional variation in the solar insolation but damped by the local feedback from the outgoing radiation and the meridional mixing because of the monsoon overturning circulation. For the case with a zonally confined land, the land surface is remotely influenced by the ocean at similar latitudes through the westerly jet advection in the free troposphere.

An analytical solution can then be derived for ΔT_a as

$$\Delta T_a = \frac{s}{\sqrt{1+u^2}} \sin(\hat{t} - t_0). \qquad (12)$$

Here,

$$u = \left(\frac{\tau}{T}\right) 2\pi \qquad (13)$$

measures the ratio between the intrinsic time scale τ and the forcing time scale T;

$$t_0 = \tan^{-1} u \qquad (14)$$

measures the phase lag of ΔT_a relative to the sun, which increases monotonically with the slab-ocean depth H according to Eqs. (4), (8), (9), and (13). The numerator in Eq. (12)

$$s = \frac{S_o}{\gamma} \qquad (15)$$

measures the potential intensity of ΔT_a, which increases with the seasonal variation of insolation S_o. It should be noted that for tropical monsoons here,

we assume the free troposphere to be in quasi equilibrium with the surface. For the extratropics, Donohoe et al. (2014) find that the seasonal phase of the atmospheric temperature varies nonmonotonically with *H*, as the free troposphere is no longer well coupled with the surface but partially driven by the solar radiation directly. The increasing ΔT_a magnitude with S_o is consistent with the paleoclimate records of the mid-Holocene (Street and Grove 1976; Jolly et al. 1998; Haug et al. 2001).

Figure 3b shows the time evolution and intensity of ΔT_a predicted by the above analytical solution. In the limit of $u = 0$, the surface temperature achieves an equilibrium with the solar insolation instantly, and Eq. (12) reduces to $\Delta T_a = s \sin \hat{t}$. The magnitude of ΔT_a is 13 K, and it changes its sign at the March equinox (black line). This equilibrium solution can be numerically simulated (Fig. 2f) by artificially increasing the length of a year, which, together with an *H* of 0.1 m, makes the parameter *u* effectively 0 [see Eq. (13)]. The simulated ΔT_a, as shown by the black line in Fig. 3a, is consistently predicted by $\Delta T_a = s \sin \hat{t}$. According to Eq. (12), a nonzero *u* will delay and weaken ΔT_a from this simultaneous equilibrium. In the limit of vanishing surface heat capacity (blue line), the heat capacity of the moist atmosphere still leads to a considerable *u* that delays the phase of ΔT_a by about 20 days (from the equinox to mid-April) and reduces its intensity by 10%. In the limit of infinite surface heat capacity (red line), $u \to \infty$ and $\hat{t}_0 \to \pi/2$, so ΔT_a changes its sign at the summer solstice and has a very weak intensity. Overall, the linearized model (Fig. 3b) successfully explains the time evolution and intensity of the aquaplanet monsoon rainfall (Fig. 3a).

Now we look at the monsoon extent. The monsoon extent is guided by the location of the T_a maximum (Fig. 2), which is further controlled by both the annual mean and the seasonal variance of the solar insolation. The annual-mean insolation decreases with the latitude, while the seasonal variance increases with the latitude (not shown). With an infinite surface heat capacity, the effect of the seasonal variance would be completely damped, and the T_a maximum would simply stay at the equator where the annual-mean insolation is maximum. The prescribed equatorial upwelling cooling [Eq. (1)], however, sets the T_a maximum off the equator (Fig. 2a). A smaller surface heat capacity would amplify the effect of the seasonal variance of the insolation and, hence, would lead to a farther-poleward T_a maximum and monsoon rainfall (Fig. 2). For the equilibrium monsoon with $u = 0$, the T_a maximum follows the sun simultaneously and is able to reach the most poleward latitude (44°N) that the solar insolation maximum can reach (Fig. 2f). In the limit of vanishing surface heat capacity, the heat capacity of the moist atmosphere still induces a nonzero *u*, which reduces the extent of the T_a maximum from its potential extent (44°N) to about 35°N (Fig. 2e). It is also interesting to note that, although the T_a maximum extends over 30°N in cases with low surface heat capacity, most of the monsoon rainfall is limited

within the tropics (30°S–30°N), indicating a dynamical boundary for the circulation response to the surface temperature perturbation.

4. Land simulations

Based on the above aquaplanet monsoons, we now build toward more realistic monsoons by adding simple continents into the uniform slab ocean.

a. Zonally uniform moist land

A key difference between the land and the ocean is that the land has a much smaller heat capacity than the ocean. As we have seen in the aquaplanet simulations, a smaller surface heat capacity allows the surface to reach equilibrium with the solar insolation on a shorter time scale, leading to more-poleward and intensified monsoons. To investigate the effect of the different heat capacities between the land and the ocean, we consider a meridionally nonuniform slab ocean that is 0.1 m deep from 15° to 90°N and 50-m deep from 90°S to 15°N. This is identical to adding a zonally uniform land with a saturated surface, which still keeps the monsoon zonally uniform and leaves out the complexity from interactive soil moisture.

A similar configuration (but with simpler radiative/heat flux parameterizations and solstice condition) has been used in Privé and Plumb (2007a) to study meridionally nonuniform monsoon theories. In particular, they show that the monsoon rainfall peak occurs slightly equatorward of the surface θ_e maximum. Here, we wish to further understand the meridionally nonuniform monsoon based on the simpler aquaplanet monsoons that are almost analytically predictable.

As shown in Fig. 2g, the seasonal migration of the zonal-mean precipitation, surface θ_e, and surface winds can be understood as a hybrid of the Aqua0p1 and Aqua50 simulations. With a surface heat capacity of 0.1 m north of 15°N, the land surface θ_e distribution is similar to those in the Aqua0p1 simulation, with a slight equatorward displacement due to the effect of the large-scale advection from the cooler ocean, as proposed by Privé and Plumb (2007a). As a result, the extent of the summer monsoon rainfall is similar to that in the Aqua0p1 simulation. The rainfall intensity, however, is significantly weaker because the meridional temperature gradient is reduced by the warmer tropical ocean with a deeper depth of 50 m. The monsoon rainfall onset (magenta crosses in Fig. 2g), as measured by the time when the land rainfall averaged from 15° to 25°N first exceeds its annual-mean value, is also slightly delayed from that in the Aqua0p1 simulation (magenta crosses in Fig. 2e). With a surface heat capacity of 50 m south of 15°N, the winter monsoon in the SH is similar to that in the Aqua50 simulation but much stronger due to the enhanced meridional temperature gradient with the cooler NH land.

b. Zonally confined moist land

The realistic monsoon, however, does not occur over a zonally uniform land but a zonally confined land. Through idealized monsoon simulations, Xie and Saiki (1999) show that a zonally confined continent induces zonal asymmetry of the monsoon rainfall between the west and east sides of the continent. From the energetic perspective, Chou et al. (2001) point out that the advection of low moist static energy from the ocean into the continent contributes to the zonal asymmetry (together with the Rodwell–Hoskins effect) and leads to the less-poleward monsoon extent. Could such a "ventilation" effect also be understood from the surface θ_e perspective? If so, through what dynamical pathway is the surface θ_e affected by the ocean? And how can we understand the surface θ_e distribution over a zonally confined land based on those of the zonally uniform monsoons?

To investigate these questions, we consider a zonally confined moist land by restricting its zonal extent to be 100° in longitude. Figure 5b shows the spatial distribution of the summer-mean (June–August) precipitation, surface θ_e, and surface winds. Consistent with previous studies (Chou et al. 2001; Privé and Plumb 2007b), the summer monsoon rainfall extends less poleward and manifests zonal asymmetry between the west and east sides of the continent compared to that with a zonally uniform land. Both the less-poleward extent and zonal asymmetry of the monsoon rainfall are predicted by the surface θ_e (black contours). This indicates that the ocean influence on the land can be understood from the surface θ_e perspective.

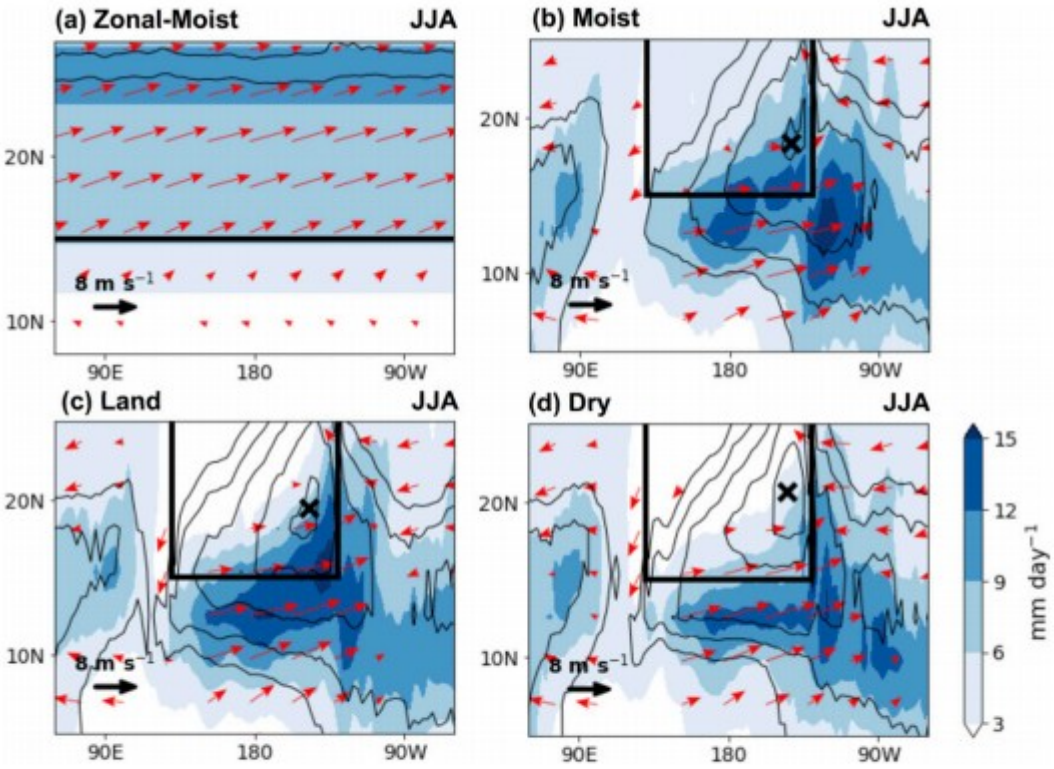

FIG. 5. Summer (JJA)-mean precipitation (shading), surface θ_e (contours), and surface winds (vectors) in simulations with (a) zonally uniform moist land, (b) zonally confined moist land, (c) zonally confined interactive land, and (d) zonally confined dry land. The black cross indicates the location of the surface θ_e maximum. The θ_e contours are plotted with an interval of 2 K starting from 348 K for (a) and from 333 K for (b)–(d). The black thick lines indicate the continent's boundary.

Here, we propose a dynamical pathway, as illustrated in Fig. 4, to explain how the ocean affects the surface θ_e distribution over the land. Figure 6a shows the θ_e difference at the surface and in the free troposphere (300 hPa) between simulations with zonally uniform land and with zonally confined land. In the summer, the NH extratropical ocean is cooler than the land at the same latitude. With a quasi-equilibrium atmosphere, this leads to a cooler free troposphere over the ocean. The cooler free-tropospheric air is advected into the land by the upper-level westerly jet. The resulting cooling in the free troposphere further cools the land surface through convective mixing, which works to maintain a convective-neutral atmosphere. As shown in Fig. 6a, the land surface cooling is stronger over the northwest continent because the westerly jet enters from the west and the ocean surface cooling relative to the land is stronger at higher latitudes. Because of this cooling effect, the surface θ_e maximum over the land moves equatorward and shows strong zonal asymmetry.

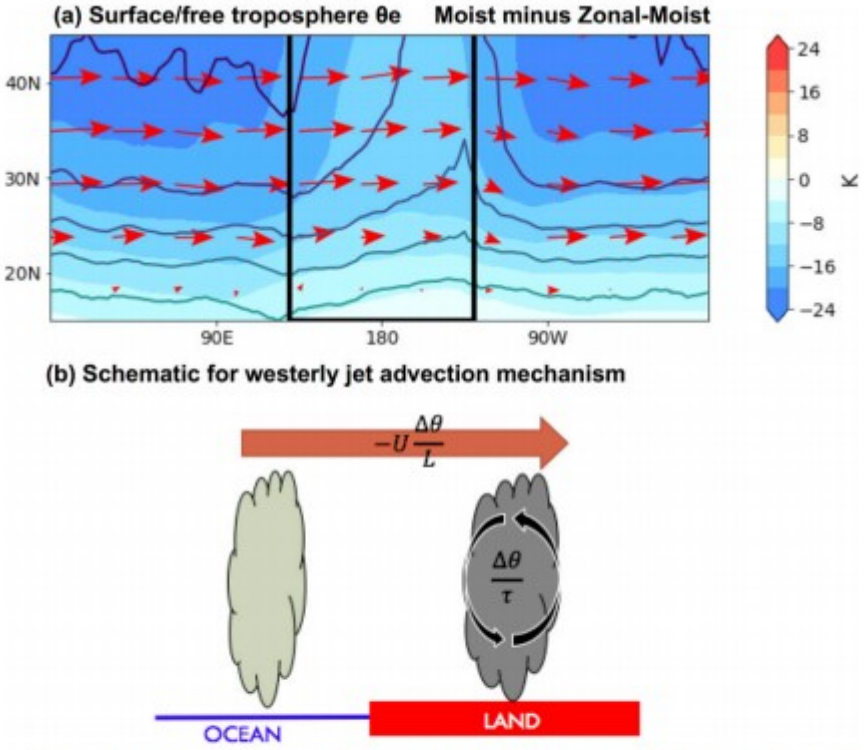

FIG. 6. (a) Summer-mean θ_e difference at the surface (contours; −10-K interval from 0 K) and in the free troposphere (shading; 300 hPa) between the Moist and Zonal-Moist simulations. The vectors show the winds at 300 hPa in the Zonal-Moist simulation. (b) Schematic for deriving a length scale of the land cooling based on the balance between the westerly jet advection and the convective mixing.

A scale for the penetration depth of the land cooling L can be derived according to the balance between the westerly jet advection and the convective mixing (see schematic in Fig. 6b). Given the surface (and the upper tropospheric) θ_e difference between the land and the ocean $\Delta\theta_e$ and the westerly jet speed U, the cooling tendency due to the westerly jet advection can be estimated as $-U\Delta\theta_e/L$. By assuming a time scale for the atmospheric adjustment to quasi equilibrium τ_o, the warming tendency on the upper troposphere from the convective mixing can be estimated as $\Delta\theta_e/\tau_o$. The balance between them then leads to a length scale for land cooling as $L \sim U\tau_o$. Given a typical westerly jet speed U = 40 m s^{-1}, and a relaxing time scale τ_o = 1 day, the above estimate leads to $L \sim 40°$ (in longitude), which is roughly consistent with the scale we observe in our simulations.

Because of such ocean influence on the land, the θ_e distribution over the zonally confined land (Moist) can be seen as a balance between that of the zonally uniform land (Zonal-Moist) and that of the uniform 50-m slab ocean (Aqua50). Indeed, the monsoon rainfall peak sits at 16°N (Fig. 5b), which is between 25°N as in the Zonal-Moist simulation (Fig. 5a) and 10°N as in the Aqua50 simulation (Fig. 2b). The monsoon rainfall onset, as measured by the time when the land rainfall averaged from 15° to 25°N first exceeds its annual-mean value, occurs in early June (magenta cross in Fig. 2h), which is

between mid-May as in the Zonal-Moist simulation (magenta cross in Fig. 2g) and early August as in the Aqua50 simulation (magenta cross in Fig. 2b).

c. Soil moisture

Besides its smaller heat capacity, the land is distinct from the ocean because of the interaction between the limited soil moisture and precipitation. It is established in both paleoclimate records (e.g., Kutzbach et al. 1996; Levis et al. 2004) and simulations (e.g., Meehl 1994; Berg et al. 2017) that the soil–moisture–precipitation interaction plays an important role in affecting both the migration and intensity of the monsoon rainfall. Here, with simplified land geometry and large-scale circulations, we investigate how the interactive soil moisture would affect the regional monsoon rainfall pattern and study how the soil moisture effect could be incorporated into the surface θ_e control on the monsoon rainfall.

We consider a simple interactive soil moisture scheme following Holloway and Manabe (1971). Soil moisture is accumulated from precipitation minus evaporation, and the surface evaporation is proportional to the soil moisture depth as follows:

$$E = \min\left(1, \frac{D_s}{0.75 D_{so}}\right) E_P \quad \text{and} \qquad (16)$$

$$\frac{dD_s}{dt} = P - E, \qquad (17)$$

where E is evaporation, P is precipitation, E_P is the potential evaporation, D_s is the soil moisture depth, and D_{so} is the maximum soil moisture depth. A lower bound is set for D_s so that the land will not completely dry out in the dry season.

The time evolution of the mean surface air temperature, surface θ_e, and precipitation over the subtropical land is shown in Fig. 7a for the simulation with interactive soil moisture (Land). The surface air temperature now peaks before the monsoon rainfall as in observations. The time evolution of the monsoon rainfall is well predicted by the surface θ_e. In the tropics, the horizontal θ_e difference in the free troposphere is weak because of fast waves, so the location of strong convective instability and precipitation is mainly controlled by the surface θ_e.

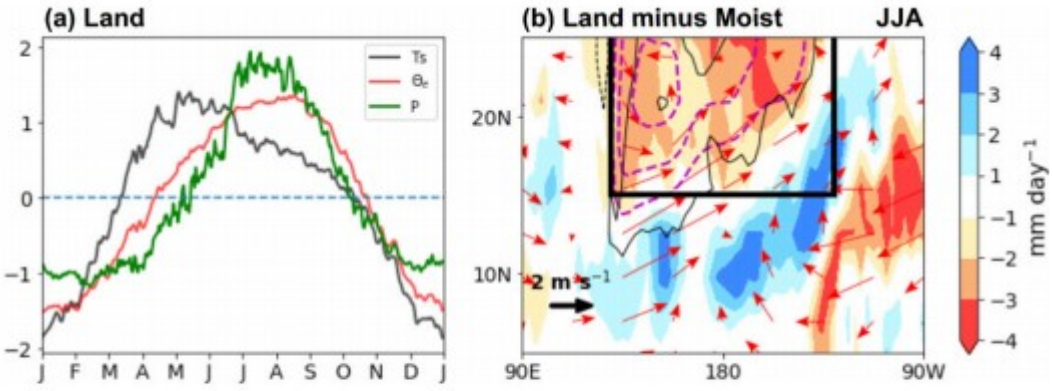

FIG. 7. (a) Time evolution of the mean surface temperature (black), surface θ_e (red), and precipitation (green) averaged over the zonally confined interactive land from 15° to 25°N relative to the tropical mean. All values are scaled by their standard deviations. (b) Difference in the summer (JJA)-mean precipitation (shading), surface θ_e (black contours at −1, 1, and 2 K), surface pressure (magenta contours at −4, −3, and −2 hPa) and surface winds (vectors) between the simulation with an interactive soil moisture scheme and that with a moist land.

Figure 7b shows the difference in the summer-mean precipitation, surface θ_e, surface pressure, and surface winds between the simulation with an interactive soil moisture scheme and that with a moist land. While the summer monsoon rainfall is overall reduced inland because of the limited soil moisture, it is also locally enhanced over the southeast continent. The drier land surface induces warmer surface temperature and lower surface pressure. The associated surface southwesterly winds transport moisture inland and enhance the precipitation over the southeast continent where the soil moisture is already close to saturation.

To understand how the soil moisture effect could be incorporated into the surface θ_e perspective, we further consider a case of dry land, in which soil moisture is fixed at a low value such that actual evaporation is reduced to 10% of the potential evaporation. As the land changes from moist (Fig. 5b), to interactive (Fig. 5c), to dry (Fig. 5d), the θ_e maximum moves poleward (black cross) because of the higher land surface temperature, but the summer monsoon rainfall retreats equatorward. This indicates that the general rule that precipitation follows the θ_e maximum no longer holds when soil moisture is externally perturbed and emphasizes the additional control on monsoon rainfall by soil moisture. In the simulation with dry land, deep convection is suppressed such that the land surface becomes thermodynamically decoupled from the free troposphere. This breaks the quasi-equilibrium assumption and consequently fails the general guide of the surface θ_e maximum on monsoon rainfall.

d. Land geometry

Monsoon rainfall is known to be affected by land geometry. Dirmeyer (1998) finds that the monsoon is sensitive to the climatological zone in which the continent is located. The longitudinal extent of the continent is shown to have a substantial impact on the large-scale tropical rainfall (Maroon et al. 2016; Maroon and Frierson 2016). As we show in section 4b, the

surface θ_e and monsoon rainfall over the zonally confined continent are substantially modulated by the ocean. Land geometry is expected to affect both the pathway and the relative importance of the ocean influence. Here, we investigate such land geometry impact by perturbing the width and the south and north edges of the continent.

As the land becomes wider, the summer monsoon rainfall extends farther inland with a more-poleward θ_e maximum (Figs. 8a,b). With the penetration depth of land cooling approximately set by the westerly jet speed and the temperature contrast between the ocean and the land (see section 4b), a wider land reduces the relative importance of the ocean influence on the land and, hence, leads to a farther poleward θ_e maximum that is closer to that in the zonally uniform land case.

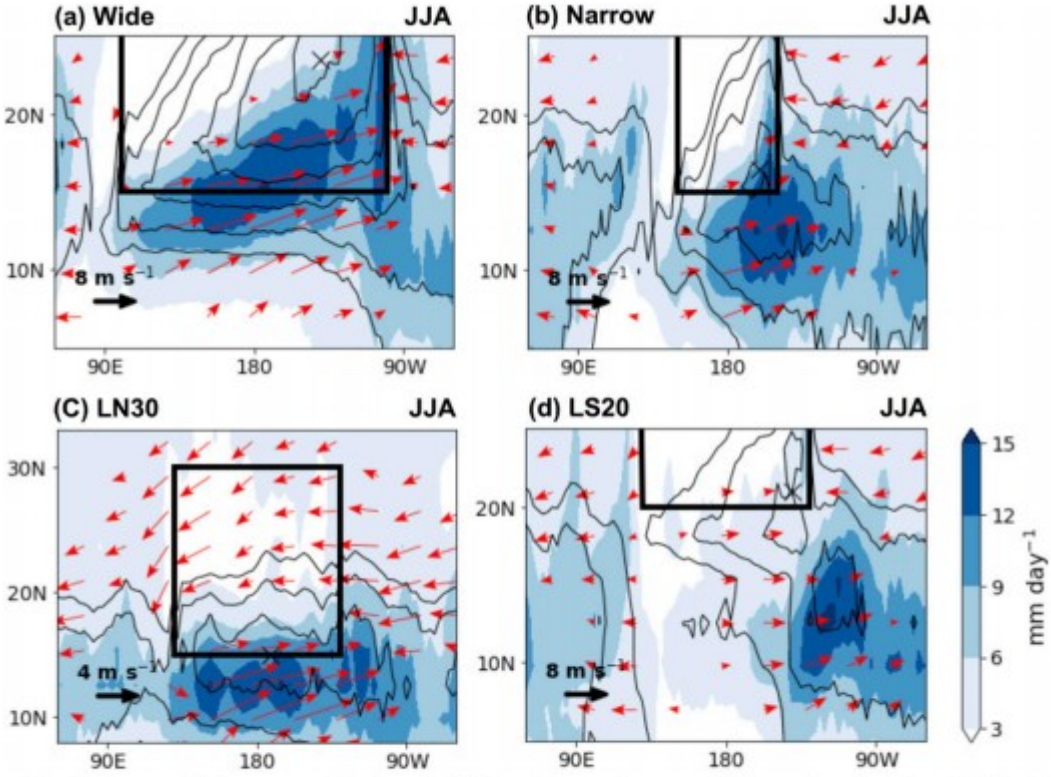

FIG. 8. Summer (JJA)-mean precipitation (shading), surface θ_e (contours; 2-K interval starting from 333 K) and surface winds (vectors) in zonally confined land simulations with (a) wider land, (b) narrow land, (c) land with a north edge at 30°N, and (d) land with a south edge from 20°N. The black cross indicates the location of the surface θ_e maximum. Please note that the latitude range in (c) is different from others.

Lowering the north edge of the land to 30°N leads to an equatorward retreat of the summer monsoon rainfall as the additional advection of the cooler air from the surrounding oceans pushes the surface θ_e maximum over the land equatorward (Fig. 8c). The zonal rainfall asymmetry is nearly eliminated with horizontal contours of the surface θ_e. The reduced monsoon extent with a lower north edge may explain why monsoon rainfalls over Australia and West Africa, whose poleward edges are also at ~30°, only reach ~12° with the surface θ_e maximum locating at ~15° (Figs. 1b,c).

Raising the south edge of the land to 20°N almost eliminates the monsoon (Fig. 8d). Privé and Plumb (2007a) show that the response of the cross-equatorial Hadley circulation to the subtropical forcing weakens sharply as the forcing shifts poleward and passes a certain threshold latitude. This helps explain why there is no obvious monsoon as the θ_e maximum locates rather poleward with a weak magnitude.

5. Local and remote forcings

Besides the above physical parameters, monsoon rainfall can be sensitive to local (land use, vegetation) and remote (SST) forcings. Here, the response of the monsoon rainfall to local forcing is investigated by perturbing the surface albedo of the zonally confined land. With increased surface albedo, the surface θ_e maximum over the land decreases and moves equatorward, leading to weakened monsoon rainfall with reduced inland extent (Figs. 9a,b). Over a wide range of albedo change, both the extent and intensity of the monsoon rainfall decrease nearly linearly with the land albedo (Figs. 9c,d), which is consistent with previous studies with more realistic configurations (Boos and Storelvmo 2016).

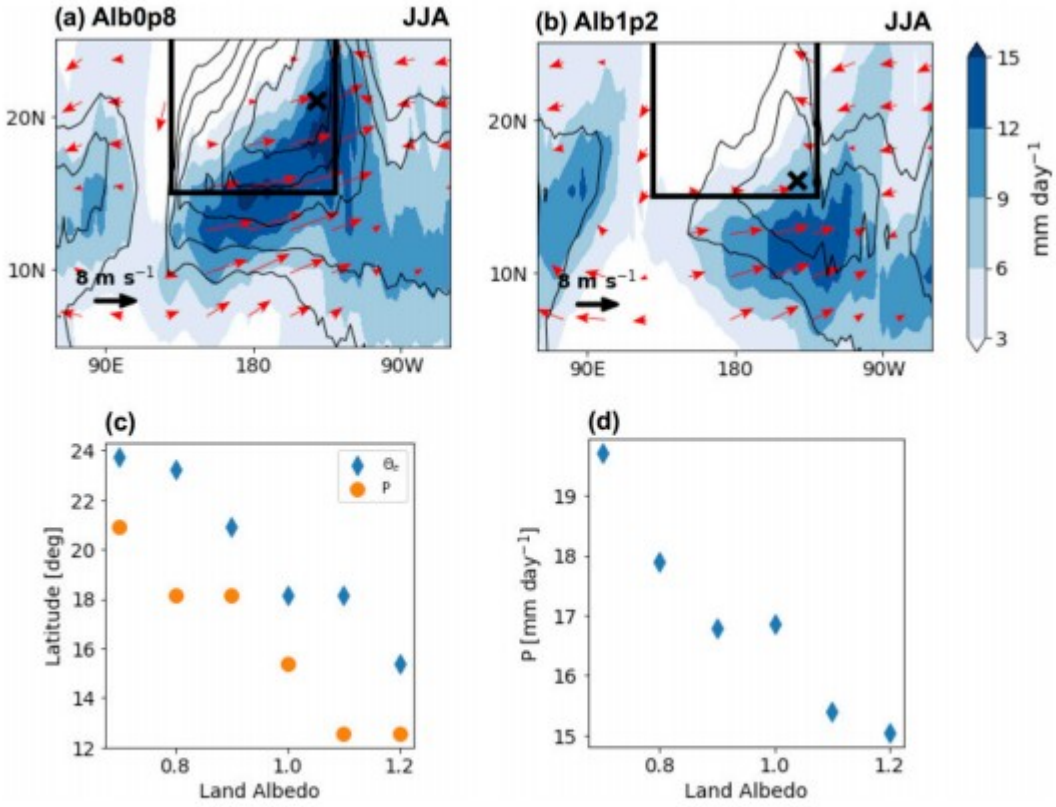

FIG. 9. The summer-mean precipitation (shading), surface θ_e (contours; 2-K interval from 333 K), surface winds (vectors) in the (a) Alb0p8 simulation with decreased land albedo and (b) Alb1p2 simulation with increased land albedo. (c) Scatterplot of the land albedo perturbation vs the latitude of the surface θ_e maximum and the precipitation peak. (d) Scatterplot of the land albedo vs the maximum precipitation rate.

The response of the monsoon rainfall to remote forcing is investigated by adding the following surface heat flux anomaly over the ocean:

$$\mathrm{NH-Flx} = Q_o \sin\left(\frac{\varphi - 40^\circ}{50^\circ}\pi\right) \quad \text{for } 40^\circ < \varphi < 90^\circ$$

or

$$\mathrm{SH-Flx} = Q_o \sin\left(\frac{\varphi + 40^\circ}{50^\circ}\pi\right) \quad \text{for } -90^\circ < \varphi < -40^\circ,$$

where φ is the latitude (°) and Q_o = 60 W m^{-2}. The heat flux anomaly either warms the midlatitude NH oceans or cools the midlatitude SH oceans, adding interhemispheric asymmetry into the system. According to the energetic perspective (Broccoli et al. 2006; Kang et al. 2008, 2009; Yoshimori and Broccoli 2009; Frierson and Hwang 2012; Frierson et al. 2013; Schneider et al. 2014; Boos and Korty 2016), this would imply an anomalous cross-equatorial circulation response that offsets the imposed energy asymmetry and presumably induces changes in the monsoon rainfall. However, as shown in Fig. 10, despite imposing a similar interhemispheric asymmetry, the NH warming and the SH cooling lead to distinct monsoon rainfall changes. In response to the NH warming, the summer monsoon rainfall intensifies and extends farther inland (Fig. 10a); in contrast, the SH cooling barely affects the summer monsoon rainfall (Fig. 10b). Such difference can be explained from the surface θ_e perspective: The warmer NH midlatitude ocean leads to a farther inland surface θ_e maximum (Fig. 10a) through the westerly advection mechanism as discussed in section 4b; the SH ocean cooling, however, has a negligible impact on the surface θ_e over the NH continent (Fig. 10b).

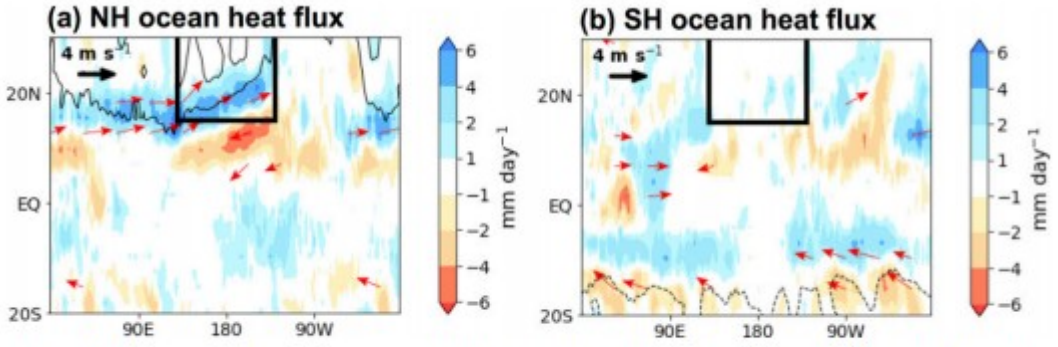

FIG. 10. The response of summer-mean precipitation (shading), surface θ_e (contours; 2-K interval ±2 K), and surface winds to the (a) NH warming and (b) SH cooling ocean heat flux.

6. Summary

A gap in understanding monsoon dynamics exists between climate models that seek to represent the full complexity of physics and theories that may be overly idealized. To bridge this gap, a hierarchy of idealized monsoons with increased degrees of complexity has been built using an intermediate moist GCM with simplified physics and geometries. As illustrated in Fig. 11, a

basic understanding of monsoon features such as the extent, intensity, and time evolution has been formulated based on this hierarchy of idealized monsoons by studying how the distribution of the surface equivalent potential temperature θ_e, which proves to well guide the monsoon rainfall, is modified step by step as new complexity is introduced into the system.

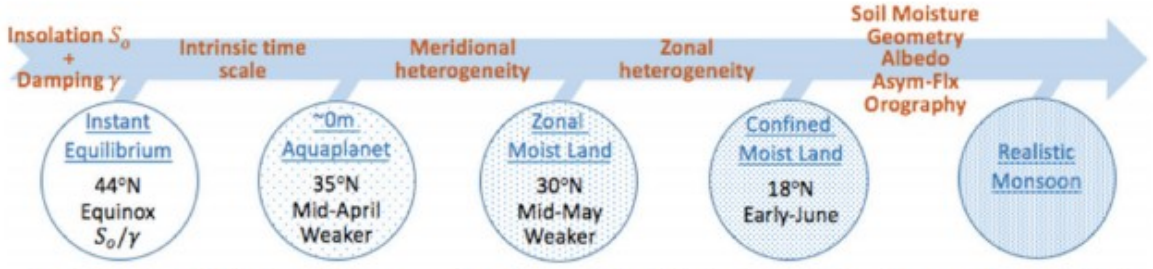

FIG. 11. Steps from idealized to realistic monsoons by adding complexity. The latitude values indicate the most-poleward latitude that the zonal-/sector-mean θ_e maximum could reach. The time values are either the shift time of the monsoon rainfall from the SH to the NH in the aquaplanet simulations or the monsoon rainfall onset time in the land simulations.

We start from the simplest aquaplanet monsoon by forcing a uniform slab ocean with seasonally varying solar insolation. The extent, intensity, and time evolution of the monsoon rainfall is well guided by the surface θ_e maximum, which, with a saturated surface, can be understood from the meridional distribution of the surface air temperature. A linearized model about the meridional distribution of θ_e is built as driven by the seasonally varying insolation and damped by the monsoon overturning circulation and the local feedback. If the surface achieved an equilibrium instantaneously, the surface θ_e maximum would follow the sun simultaneously, shifting from the SH to the NH at the summer equinox, extending to the most-poleward latitude that the insolation maximum can reach (44°N), and with an intrinsic intensity determined by the balance between the solar insolation and the damping. This instant equilibrium is, however, mediated by an intrinsic time scale for the surface to achieve an equilibrium, which delays the monsoon evolution and reduces the monsoon intensity and extent. Even in the limit of vanishing surface heat capacity, the finite heat capacity of the moist atmosphere delays the monsoon evolution by about 20 days, reduces the monsoon extent to about 30°N, and weakens the monsoon intensity by 10%.

The simplest aquaplanet monsoon is further modified by the meridional and zonal heterogeneity in the surface heat capacity. The zonally uniform but meridionally nonuniform monsoon can be seen as a hybrid of the aquaplanet monsoons. With a zonally confined moist land, the land surface is cooled by the ocean through the westerly jet advection in the free troposphere and the convective mixing that tends to maintain a convective-neutral atmosphere. The θ_e maximum moves to a lower latitude, leading to a reduced inland extent of the monsoon rainfall. As the westerly jet enters from the west, the land cooling is enhanced on the west side of the continent, leading to zonal

asymmetry of the monsoon rainfall. The land geometry plays an important role in shaping the monsoon rainfall distribution by controlling the pathway and the relative importance of the ocean influence on the land.

Building toward more realistic monsoons, we allow the soil moisture to interact with precipitation. Although monsoon rainfall is reduced inland because of limited soil moisture, the warmer inland surface temperature induces regional circulation that leads to locally enhanced rainfall over the southeast continent.

The relationship between the locations of the surface θ_e maximum and the monsoon rainfall peak is summarized for all experiments in Fig. 12. In general, the monsoon rainfall peak is well guided by the surface θ_e maximum except when the soil moisture is externally varied, which plays as an additional control on monsoon rainfall.

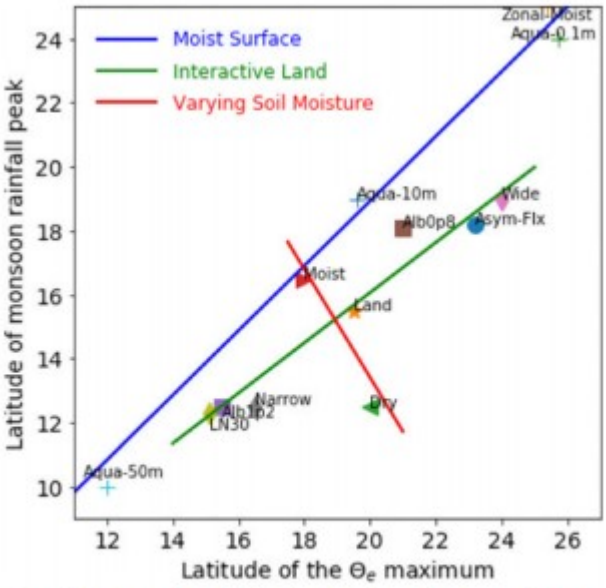

FIG. 12. Scatterplot of the latitude of the surface θ_e maximum vs the latitude of the monsoon rainfall peak in the summer. See Table 1 for detailed experiment descriptions.

Finally, it is worthwhile to note a few limitations of using an intermediate GCM with simplified physics. First, by assuming a gray atmosphere, the model neglects the interaction among water vapor, cloud, and radiation. Second, the relative coarse horizontal and vertical resolutions used here are not likely to well represent processes such as the shallow meridional circulation (Peyrille and Lafore 2007; Zhang et al. 2008; Thorncroft et al. 2011; Zhai and Boos 2017). Both mechanisms have certain impacts on the monsoon rainfall. Another important process that is not included here is the topography, which could affect the θ_e maxima through either elevated heating (e.g., Wu et al. 2012; Hu and Boos 2017) or by blocking the advection of low-θ_e air (e.g., Boos and Kuang 2010; Molnar et al. 2010). Although we feel that the basic understanding of the θ_e distribution

illustrated here will still hold, it is worthwhile for future studies to investigate the effect of more realistic complexity.

Acknowledgments

This work is supported by the National Science Foundation (Grant 1637450). Numerical simulations are conducted using the computing resources provided by both GFDL and NCAR.

REFERENCES

Adler, R. F., and Coauthors, 2003: The version-2 Global Precipitation Climatology Project (GPCP) monthly precipitation analysis (1979–present). *J. Hydrometeor.*, 4, 1147–1167, https://doi.org/10.1175/1525-7541(2003)004<1147:TVGPCP>2.0.CO;2.

Berg, A. M., B. R. Lintner, K. L. Findell, and A. Giannini, 2017: Soil moisture influence on seasonality and large-scale circulation in simulations of the West African monsoon. *J. Climate*, 30, 2295–2317, https://doi.org/10.1175/JCLI-D-15-0877.1.

Boos, W. R., and Z. Kuang, 2010: Dominant control of the South Asian monsoon by orographic insulation versus plateau heating. *Nature*, 463, 218–222, https://doi.org/10.1038/nature08707.

Boos, W. R., and R. L. Korty, 2016: Regional energy budget control of the intertropical convergence zone and application to mid-Holocene rainfall. *Nat. Geosci.*, 9, 892–897, https://doi.org/10.1038/ngeo2833.

Boos, W. R., and T. Storelvmo, 2016: Near-linear response of mean monsoon strength to a broad range of radiative forcings. *Proc. Natl. Acad. Sci. USA*, 113, 1510–1515, https://doi.org/10.1073/pnas.1517143113.

Bordoni, S., and T. Schneider, 2008: Monsoons as eddy-mediated regime transitions of the tropical overturning circulation. *Nat. Geosci.*, 1, 515–519, https://doi.org/10.1038/ngeo248.

Broccoli, A. J., K. A. Dahl, and R. J. Stouffer, 2006: Response of the ITCZ to Northern Hemisphere cooling. *Geophys. Res. Lett.*, 33, L01702, https://doi.org/10.1029/2005GL024546.

Chao, W. C., and B. Chen, 2001: The origin of monsoons. *J. Atmos. Sci.*, 58, 3497–3507, https://doi.org/10.1175/1520-0469(2001)058<3497:TOOM>2.0.CO;2.

Chou, C., and J. D. Neelin, 2001: Mechanisms limiting the southward extent of the South American summer monsoon. *Geophys. Res. Lett.*, 28, 2433–2436, https://doi.org/10.1029/2000GL012138.

Chou, C., J. D. Neelin, and H. Su, 2001: Ocean–atmosphere–land feedbacks in an idealized monsoon. *Quart. J. Roy. Meteor. Soc.*, 127, 1869–1891, https://doi.org/10.1002/qj.49712757602.

Cronin, T. W., and K. A. Emanuel, 2013: The climate time scale in the approach to radiative-convective equilibrium. *J. Adv. Model. Earth Syst.*, 5, 843–849, https://doi.org/10.1002/jame.20049.

Dee, D. P., and Coauthors, 2011: The ERA-Interim reanalysis: Configuration and performance of the data assimilation system. *Quart. J. Roy. Meteor. Soc.*, 137, 553–597, https://doi.org/10.1002/qj.828.

Dima, I. M., and J. M. Wallace, 2003: On the seasonality of the Hadley cell. *J. Atmos. Sci.*, 60, 1522–1527, https://doi.org/10.1175/1520-0469(2003)060<1522:OTSOTH>2.0.CO;2.

Dirmeyer, P. A., 1998: Land-sea geometry and its effect on monsoon circulations. *J. Geophys. Res.*, 103, 11 555–11 572, https://doi.org/10.1029/98JD00802.

Donohoe, A., D. M. W. Frierson, and D. S. Battisti, 2014: The effect of ocean mixed layer depth on climate in slab ocean aquaplanet experiments. *Climate Dyn.*, 43, 1041–1055, https://doi.org/10.1007/s00382-013-1843-4.

Emanuel, K. A., 1995: On thermally direct circulations in moist atmospheres. *J. Atmos. Sci.*, 52, 1529–1536, https://doi.org/10.1175/1520-0469(1995)052<1529:OTDCIM>2.0.CO;2.

Frierson, D. M. W., 2007: The dynamics of idealized convection schemes and their effect on the zonally averaged tropical circulation. *J. Atmos. Sci.*, 64, 1959–1976, httsps://doi.org/10.1175/JAS3935.1.

Frierson, D. M. W., and Y.-T. Hwang, 2012: Extratropical influence on ITCZ shifts in slab ocean simulations of global warming. *J. Climate*, 25, 720–733, https://doi.org/10.1175/JCLI-D-11-00116.1.

Frierson, D. M. W., and Coauthors, 2013: Contribution of ocean overturning circulation to tropical rainfall peak in the Northern Hemisphere. *Nat. Geosci.*, 6, 940–944, https://doi.org/10.1038/ngeo1987.

Fučkar, N. S., S.-P. Xie, R. Farneti, E. A. Maroon, and D. M. W. Frierson, 2013: Influence of the extratropical ocean circulation on the intertropical convergence zone in an idealized coupled general circulation model. *J. Climate*, 26, 4612–4629, https://doi.org/10.1175/JCLI-D-12-00294.1.

Gadgil, S., 2003: The Indian monsoon and its variability. *Annu. Rev. Earth Planet. Sci.*, 31, 429–467, https://doi.org/10.1146/annurev.earth.31.100901.141251.

Gonzalez, A. O., and G. M. Rojas, 2014: Balanced dynamics of deep and shallow Hadley circulations in the tropics. *J. Adv. Model. Earth Syst.*, 6, 777–804, https://doi.org/10.1002/2013MS000278.

Haug, G. H., K. A. Hughen, D. M. Sigman, L. C. Peterson, and U. Röhl, 2001: Southward migration of the intertropical convergence zone through the Holocene. *Science*, 293, 1304–1308, https://doi.org/10.1126/science.1059725.

Held, I. M., 2005: The gap between simulation and understanding in climate modeling. *Bull. Amer. Meteor. Soc.*, 86, 1609–1614, https://doi.org/10.1175/BAMS-86-11-1609.

Held, I. M., and A. Y. Hou, 1980: Nonlinear axially symmetric circulations in a nearly inviscid atmosphere. *J. Atmos. Sci.*, 37, 515–533, https://doi.org/10.1175/1520-0469(1980)037<0515:NASCIA>2.0.CO;2.

Holloway, J. L., Jr., and S. Manabe, 1971: Simulation of climate by a global general circulation model: I. Hydrologic cycle and heat balance. *Mon. Wea. Rev.*, 99, 335–370, https://doi.org/10.1175/1520-0493(1971)099<0335:SOCBAG>2.3.CO;2.

Hu, S., and W. R. Boos, 2017: The physics of orographic elevated heating in radiative–convective equilibrium. *J. Atmos. Sci.*, 74, 2949–2965, https://doi.org/10.1175/JAS-D-16-0312.1.

Jolly, D., S. Harrison, B. Damnati, and R. Bonnefille, 1998: Simulated climate and biomes of Africa during the Late Quaternary: Comparison with pollen and lake status data. *Quat. Sci. Rev.*, 17, 629–657, https://doi.org/10.1016/S0277-3791(98)00015-8.

Kang, S. M., I. M. Held, D. M. W. Frierson, and M. Zhao, 2008: The response of the ITCZ to extratropical thermal forcing: Idealized slab ocean experiments with a GCM. *J. Climate*, 21, 3521–3532, https://doi.org/10.1175/2007JCLI2146.1.

Kang, S. M., D. M. W. Frierson, and I. M. Held, 2009: The tropical response to extratropical thermal forcing in an idealized GCM: The importance of radiative feedbacks and convective parameterization. *J. Atmos. Sci.*, 66, 2812–2827, https://doi.org/10.1175/2009JAS2924.1.

Kutzbach, J., G. Bonan, J. Foley, and S. P. Harrison, 1996: Vegetation and soil feedbacks on the response of the African monsoon to orbital forcing in the early to middle Holocene. *Nature*, 384, 623–626, https://doi.org/10.1038/384623a0.

Levine, X. J., and W. R. Boos, 2017: Land surface albedo bias in climate models and its association with tropical rainfall. *Geophys. Res. Lett.*, 44, 6363–6372, https://doi.org/10.1002/2017GL072510.

Levis, S., G. B. Bonan, and C. Bonfils, 2004: Soil feedback drives the mid-Holocene North African monsoon northward in fully coupled CCSM2 simulations with a dynamic vegetation model. *Climate Dyn.*, 23, 791–802, https://doi.org/10.1007/s00382-004-0477-y.

Lindzen, R. S., and A. Y. Hou, 1988: Hadley circulations for zonally averaged heating centered off the equator. *J. Atmos. Sci.*, 45, 2416–2427, https://doi.org/10.1175/1520-0469(1988)045<2416:HCFZAH>2.0.CO;2.

Maroon, E. A., and D. M. W. Frierson, 2016: The impact of a continent's longitudinal extent on tropical precipitation. *Geophys. Res. Lett.*, 43, 11 921–11 929, https://doi.org/10.1002/2016GL071518.

Maroon, E. A., D. M. W. Frierson, S. M. Kang, and J. Scheff, 2016: The precipitation response to an idealized subtropical continent. *J. Climate*, 29, 4543–4564, https://doi.org/10.1175/JCLI-D-15-0616.1.

Meehl, G. A., 1994: Influence of the land surface in the Asian summer monsoon: External conditions versus internal feedbacks. *J. Climate*, 7, 1033–1049, https://doi.org/10.1175/1520-0442(1994)007<1033:IOTLSI>2.0.CO;2.

Merlis, T. M., T. Schneider, S. Bordoni, and I. Eisenman, 2013: Hadley circulation response to orbital precession. Part II: Subtropical continent. *J. Climate*, 26, 754–771, https://doi.org/10.1175/JCLI-D-12-00149.1.

Molnar, P., W. R. Boos, and D. S. Battisti, 2010: Orographic controls on climate and paleoclimate of Asia: Thermal and mechanical roles for the Tibetan Plateau. *Annu. Rev. Earth Planet. Sci.*, 38, 77–102, https://doi.org/10.1146/annurev-earth-040809-152456.

Neelin, J. D., 2007: Moist dynamics of tropical convection zones in monsoons, teleconnections and global warming. *The Global Circulation of the Atmosphere*, T. Schneider and A. H. Sobel, Eds., Princeton University Press, 267–301.

Nie, J., W. R. Boos, and Z. Kuang, 2010: Observational evaluation of a convective quasi-equilibrium view of monsoons. *J. Climate*, 23, 4416–4428, https://doi.org/10.1175/2010JCLI3505.1.

Nilsson, J., and K. A. Emanuel, 1999: Equilibrium atmospheres of a two-column radiative convective model. *Quart. J. Roy. Meteor. Soc.*, 125, 2239–2264, https://doi.org/10.1002/qj.49712555814.

O'Gorman, P. A., and T. Schneider, 2008: The hydrological cycle over a wide range of climates simulated with an idealized GCM. *J. Climate*, 21, 3815–3832, https://doi.org/10.1175/2007JCLI2065.1.

Peyrille, P., and J. P. Lafore, 2007: An idealized two-dimensional framework to study the West African monsoon. Part II: Large-scale advection and the diurnal cycle. *J. Atmos. Sci.*, 64, 2783–2803, https://doi.org/10.1175/JAS4052.1.

Plumb, R., and A. Hou, 1992: The response of a zonally symmetric atmosphere to subtropical forcing: Threshold behavior. *J. Atmos. Sci.*, 49, 1790–1799, https://doi.org/10.1175/1520-0469(1992)049<1790:TROAZS>2.0.CO;2.

Privé, N. C., and R. A. Plumb, 2007a: Monsoon dynamics with interactive forcing. Part I: Axisymmetric studies. *J. Atmos. Sci.*, 64, 1417–1430, https://doi.org/10.1175/JAS3916.1.

Privé, N. C., and R. A. Plumb, 2007b: Monsoon dynamics with interactive forcing. Part II: Impact of eddies and asymmetric geometries. *J. Atmos. Sci.*, 64, 1431–1442, https://doi.org/10.1175/JAS3917.1.

Rodwell, M., and B. Hoskins, 1996: Monsoons and the dynamics of deserts. *Quart. J. Roy. Meteor. Soc.*, 122, 1385–1404, https://doi.org/10.1002/qj.49712253408.

Schneider, T., T. Bischoff, and G. H. Haug, 2014: Migrations and dynamics of the intertropical convergence zone. *Nature*, 513, 45–53, https://doi.org/10.1038/nature13636.

Street, F. A., and A. Grove, 1976: Environmental and climatic implications of Late Quaternary lake-level fluctuations in Africa. *Nature*, 261, 385–390, https://doi.org/10.1038/261385a0.

Thorncroft, C. D., H. Nguyen, C. Zhang, and P. Peyrille, 2011: Annual cycle of the West African monsoon: Regional circulations and associated water vapour transport. *Quart. J. Roy. Meteor. Soc.*, 137, 129–147, https://doi.org/10.1002/qj.728.

Wu, G., Y. Liu, B. He, Q. Bao, A. Duan, and F.-F. Jin, 2012: Thermal controls on the Asian summer monsoon. *Sci. Rep.*, 2, 404, https://doi.org/10.1038/srep00404.

Xie, S.-P., and N. Saiki, 1999: Abrupt onset and slow seasonal evolution of summer monsoon in an idealized GCM simulation. *J. Meteor. Soc. Japan*, 77, 949–968, https://doi.org/10.2151/jmsj1965.77.4_949.

Yoshimori, M., and A. J. Broccoli, 2009: On the link between Hadley circulation changes and radiative feedback process. *Geophys. Res. Lett.*, 36, L20703, https://doi.org/10.1029/2009GL040488.

Zhai, J., and W. R. Boos, 2017: The drying tendency of shallow meridional circulations in monsoons. *Quart. J. Roy. Meteor. Soc.*, 143, 2655–2664, https://doi.org/10.1002/qj.3091.

Zhang, C., D. S. Nolan, C. D. Thorncroft, and H. Nguyen, 2008: Shallow meridional circulations in the tropical atmosphere. *J. Climate*, 21, 3453–3470, https://doi.org/10.1175/2007JCLI1870.1.

Zhou, W., and S.-P. Xie, 2017: Intermodel spread of the double-ITCZ bias in coupled GCMs tied to land surface temperature in AMIP GCMs. *Geophys. Res. Lett.*, 44, 7975–7984, https://doi.org/10.1002/2017GL0